Monte Carlo study of the honeycomb structure of anthraquinone molecules on Cu(111)

Kwangmoo Kim and T. L. Einstein

Phys. Rev. B **83**, 245414 — Published 21 June 2011

DOI: 10.1103/PhysRevB.83.245414

Monte Carlo study of the honeycomb structure of anthraquinone molecules on Cu(111)

Kwangmoo Kim and T. L. Einstein
Department of Physics, University of Maryland, College Park, Maryland 20742-4111, USA

Using Monte Carlo calculations of the two-dimensional (2D) triangular lattice gas model, we demonstrate a mechanism for the spontaneous formation of honeycomb structure of anthraquinone (AQ) molecules on a Cu(111) plane. In our model long-range attractions play an important role, in addition to the long-range repulsions and short-range attractions proposed in Science **313**, 961 (2006). We provide a global account of the possible combinations of long-range attractive coupling constants which lead to a honeycomb superstructure. We also provide the critical temperature of disruption of the honeycomb structure and compare the critical local coverage rate of AQ's where the honeycomb structure starts to form with the experimental observations.

PACS numbers: 68.43.Hn,68.43.De,05.70.Np,73.20.-r

I. INTRODUCTION

The self-assembly of some adsorbed molecules on surfaces has garnered considerable interest. Examples include DNA-base molecules,[1] thiol molecules,[2] oligomers,[3] tetrahydroxyquinone molecules,[4] rubrenes.[5] This phenomenon has many useful applications such as in nanoscale molecular devices[6–8] and in patterning of films.[9–13]

Pawin *et al.*[14] observed the spontaneous formation of honeycomb structures of anthraquinone (AQ) molecules on a Cu(111) surface at temperatures between 10 and 200 K with local coverages above $\sim$ 15 molecules per 1000 substrate Cu atoms. The "diameter" of one hexagon is about 50 Å, which is rather large compared to the constituent molecules. Hydrogen bonding apparently occurs between oxygens of each AQ and hydrogens of neighboring AQ's. Pawin *et al.* claimed that this spontaneous formation is due to the balance between short-range attractions and long-range repulsions.

The interplay between attractions and repulsions has been widely used for decades to explain many self-organized structures. They can be a 2D dipolar lattice gas,[15] a 2D dipolar Ising model without vacancies[16–21] and with random vacancies,[22] a 2D frustrated system,[23] a bidimensional fluid system,[24] a 2D quantum Heisenberg model,[25] a density anomaly,[26] a spin-glass state,[27] correlations in fluids,[28] compositional patterns on bulk-immiscible alloy films,[29] and a colloidal fluid.[30] Our work is also based on this method. Balancing attractions and repulsions appropriately, we can get the particular lattice structure we want.

The object of this work is to simulate with Monte Carlo (MC) the spontaneous self-organization of AQ's on a Cu(111) surface in the framework of a rather simple lattice gas model. While the highly regular honeycomb structure observed in Ref. 14 is most dramatic, we will also consider the straight branches budding out from the vertices of hexagons into regions of lower coverage. Our challenge is to find possible combinations of interactions which produce the honeycomb structure and straight branches. We then seek the transition temperature from the honeycomb structure to a disordered state, i. e., we determine the phase diagram. Furthermore, we compare the percentage of hexagons as a function of the local coverage in our model with that in Ref. 14 through an appropriate mapping.

The remainder of this paper is organized as follows. Section II presents the formalism. In this section, we provide the Hamiltonian of our system, mappings of our system to the lattice gas model, and Monte Carlo (MC) calculations of the conserved-order-parameter model, the non-local algorithm. Section III presents our numerical results from the MC calculations. We discuss our results and present our conclusions in Sec. IV.

II. FORMALISM

The Hamiltonian of our system is from the lattice gas model combined with the competition between attractions and repulsions. It has the general form[15]

$$\begin{aligned}\mathcal{H} \;=\; & -\sum_{\langle ij[k]\rangle_\alpha} E_\alpha n_i n_j [n_k] + A \sum_{\langle ij\rangle}{}' \frac{n_i n_j}{|\mathbf{R}_i - \mathbf{R}_j|^3} \\ & -\mu \sum_i n_i, \end{aligned} \tag{1}$$

where n_i is the occupation number (0 or 1) of site i, E_α is a two or three adsorbate interaction energy (with the E_α assumed to be positive; the leading minus sign indicates that these interactions are attractive), $\mathbf{R}_i$ is the position vector of the site i, and μ is the chemical potential. The positive coupling constant A gives the strength of the long-range $|\mathbf{R}|^{-3}$ dipolar interactions due to electrostatic and elastic repulsions.[15–21] The $'$ in the second sum means that $i = j$ term is excluded, and $\langle ij[k]\rangle$ in the first term can be three- or more-site interactions[31,32] as well as pairwise interactions.[32]

Experimentally, in a single hexagon there are three AQ molecules on a side, with a shared vertex of pinwheel shape also composed of three AQ's as shown in Fig. 1(b). The most straightforward way to simplify the experimental structure is to map one AQ molecule to one occupied site in our triangular lattice. (This procedure is reminiscent of Berker's prefacing transformation.[33]) Then we need some fundamental interactions between sites. To do that we divide the attractive coupling constant in Eq. (1) into several terms, the nearest-neighbor attraction E_1, the linear trio attraction $E_{\rm LT}$, the isosceles trio attraction $E_{\rm IT}$, and the long-range attractions E_6, E_{12}, or E_{19}. E_6, E_{12}, and E_{19} are the attractions from the sixth, twelfth, and nineteenth nearest-neighbors, respectively. They are $2\sqrt{3}a$, where a is the lattice constant, $3\sqrt{3}a$, and $4\sqrt{3}a$, respectively, away from the reference site as in Fig. 1. We also posit an equilateral trio repulsion, without which a clustered domain appears. This is because only one type of pinwheel is observed experimentally. All the other three types are not observed as in Fig. 2. These three not observed pinwheels are derived from an AQ dimer which is a part of a side of an AQ hexagon. Since AQ's are on Cu(111) to align along the principal axes of Cu, there are only three allowed configurations which the third AQ can have. They are not just from a mere contemplation of O–H hydrogen bonds and H–H steric repulsion. Therefore Eq. (1) becomes

$$\begin{aligned}\mathcal{H} = &-E_1 \sum_{\langle ij\rangle_1} n_i n_j - E_{\rm LT} \sum_{\langle ijk\rangle_{\rm LT}} n_i n_j n_k \\ &-E_{\rm IT} \sum_{\langle ij\ell\rangle_{\rm IT}} n_i n_j n_\ell - E_6 \sum_{\langle ip\rangle_6} n_i n_p + E_{\rm T} \sum_{\langle i\ell m\rangle_{\rm T}} n_i n_\ell n_m \\ &+A \sum_{\langle ij\rangle}{}' \frac{n_i n_j}{|\mathbf{R}_i - \mathbf{R}_j|^3} - \mu \sum_i n_i, \end{aligned} \tag{2}$$

where E_6 can be replaced with E_{12} or E_{19}.

For atoms chemisorbed on metals, it is now possible in many cases to compute the shorter-range interactions like E_1 and $E_{\rm LT}$.[34–37] However, in our problem, the adsorbates are relatively large (from a physics perspective) organic molecules, and adsorption is primarily based on van der Waals bonding. To the best of our knowledge, benzene on Cu(111) is the largest molecule on a metal substrate for which lateral interactions have been computed from first principles.[38] We did gauge the size of E_1 by computing the attraction between unsupported AQ molecules at the proper orientation and separation with hybrid Hartree-Fock DFT using the CBSB7 basis with the B3LYP functional within *Gaussian 03*. This approach is generally satisfactory for H-bonding. The resulting rough estimate of E_1 was 0.15 eV, but we did not take basis set superposition error (BSSE) into account in this crude computation.

The long-range attractions are attributed to indirect interactions mediated by the Shockley surface states on the (111) facet of a noble metals such as Cu. In the asymptotic limit, these experimentally observed[39,40] oscillatory interactions take the form[41]

$$E_{\rm pair}^{\rm asym}(R) \propto -\left(\frac{4\epsilon_{\rm F}}{\pi^2}\right) \frac{\sin(2k_{\rm F}R + 2\Theta)}{(k_{\rm F}R)^2}, \tag{3}$$

where R is the interatomic separation, Θ is the effective interaction phase shift, $k_{\rm F}$ the Fermi wavevector (0.21 Å^{-1} for Cu) of the isotropic surface state, and $\epsilon_{\rm F}$ the Fermi energy (0.38 eV for Cu). The proportionality constant gives the consequences of scattering into bulk states.[41] The very slow R^{-2} decay of these interactions allow them to play a role at large separations. These interactions have been invoked to explain remarkable behavior in several surface systems.[39,40,42] Early on, one of us noted that the distance across the hexagonal pore in the experiment[14] corresponds to a minimum of Eq. (3).

Given the large number of possible interactions and the difficulty in computing all but those of shortest range, we thought it wisest to conduct this initial study in terms of a minimal set of generic parameters. The interactions that we include should be viewed as effective interactions which incorporate some effects of omitted interactions as well as the neglected degrees of freedom due to replacing organic molecules by simple "atoms". The theme, then, is to find what range of these manageable effective interactions can reproduce the salient features observed in the experiment.

In our system $\sum_i n_i$ is a constant with a given particle density, so this is called a *conserved-order-parameter (COP) model* since $s_i = 2n_i - 1$, $s_i = \pm 1$ in the equivalent Ising model. To deal with the COP model, we can use the "Kawasaki algorithm."[43] We choose at random a pair of adjacent spins, then propose to exchange their values. To

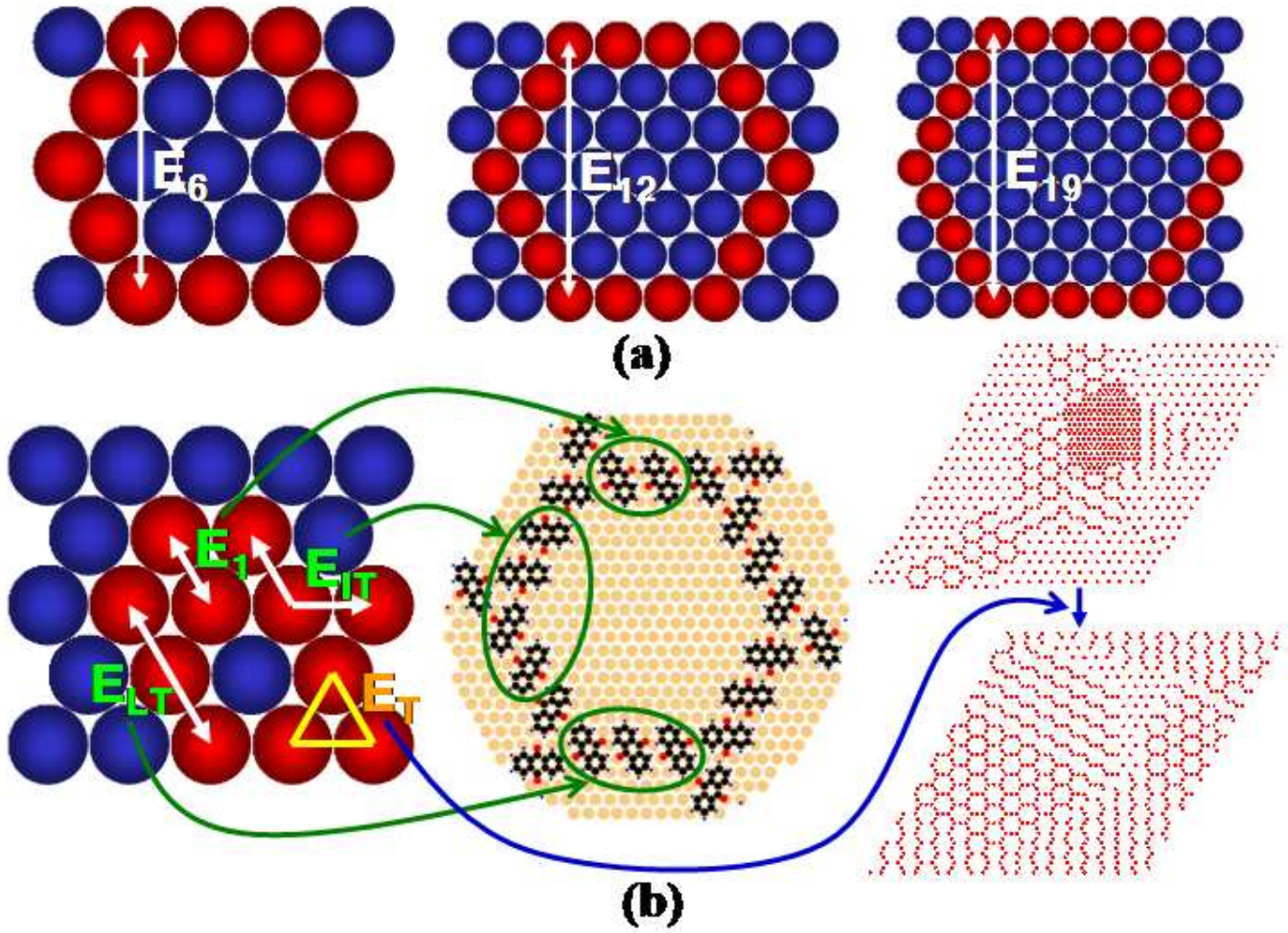

FIG. 1: (Color online) (a) Long-range attractions E_6, E_{12}, and E_{19} and (b) mappings of the attractive coupling constants (E_1, E_{LT}, E_{IT}) and the trio repulsion constant (E_{T}). Without the trio repulsion, very dense, compact clusters appear, contrary to experiment.

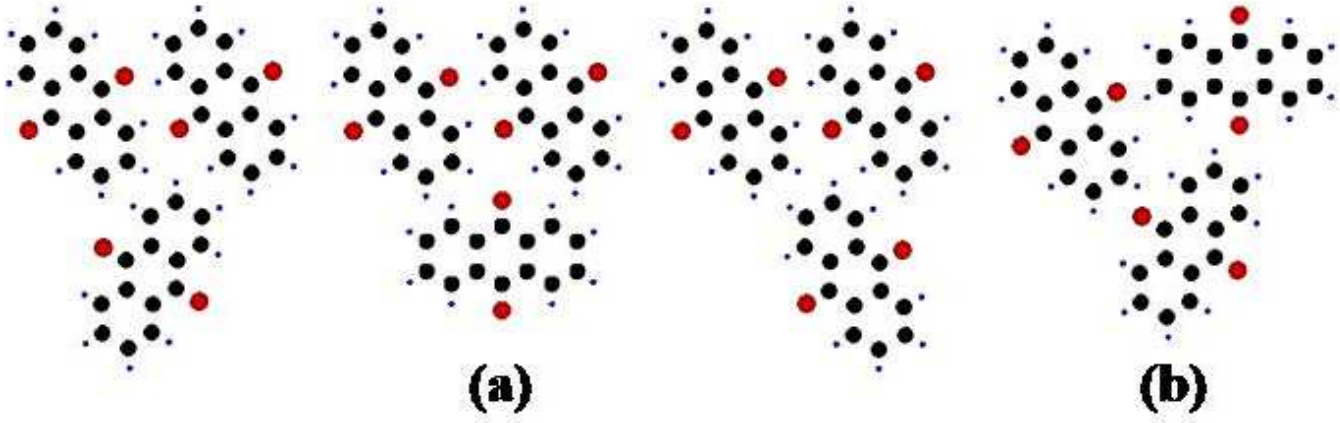

FIG. 2: (Color online) Pinwheels experimentally (a) not observed and (b) observed. Note that they are on Cu(111).

decide whether to accept this exchange or not, we calculate the energy change $\Delta E = E_f - E_i$ between the states i and f of our system before and after, and then follow the standard Metropolis acceptance probability

$$A(i \to f) = \begin{cases} e^{-\beta \Delta E} & \text{if } \Delta E > 0 \\ 1 & \text{otherwise.} \end{cases} \tag{4}$$

The implementation of the Kawasaki algorithm is not difficult, but this algorithm only moves a particle one lattice spacing at a time, so it is slow if the particles have to move a long distance. Since we are interested only in equilibrium results (not the dynamics), we do not need to confine ourselves to such local MC moves; we can do better with non-local moves.

In the "non-local algorithm,"[43] we choose two lattice sites at random and exchange their spins with the probability given in Eq. (4). When we do this, there is a reasonable chance that the two chosen spins are aligned (i. e., both occupied or both vacant in the lattice gas model), so that exchanging them is unproductive. For randomly chosen spins the probability of their being aligned is

$$p_{\parallel} = (1-\rho)^2 + \rho^2, \tag{5}$$

where the minimum value is 1/2 when $\rho = 1/2$. Therefore at least 50% of our moves are unproductive. By picking one spin from the set of up-pointing spins and one from the set of down-pointing ones and exchanging their values with Eq. (4), no move is wasted on aligned pairs of spins. This makes an immediate improvement in efficiency by a factor of $1/(1-p_{\parallel})$, which is at least 2.

The implementation of this algorithm is a little more complex than it was for the Kawasaki algorithm since we need to know where all the up- and down-spins are. In order to reap the full benefit of this algorithm, we need to keep a list of all the up- and down-spins and choose our pairs of spins at random from these lists. Since the number of up- and down-spins does not change during simulation, two arrays of fixed length can store those lists, and when the values of two spins are exchanged, we also exchange their entries in the lists. This non-local algorithm is a huge improvement over the Kawasaki algorithm for two reasons. One is the non-diffusive nature of the particle motion. The second is that the non-local update move always picks pairs of spins anti-aligned. The Kawasaki algorithm is particularly inefficient in the phase coexistence regime because most adjacent pairs of spins, which the Kawasaki algorithm only picks, are aligned in the coexistence regime. Although the non-local algorithm is more complicated to implement, it is about 20 times faster than the Kawasaki algorithm.[43]

However, this non-local algorithm is still not optimal. If the acceptance ratio is low, CPU time is wasted in selecting pairs and failing to exchange their values. These non-productive cycles can be eliminated by using a rejection-free "continuous time algorithm."[43] Since it is much more complicated to implement than the non-local algorithm and saves only about a factor of two compared to the non-local algorithm,[43] we use the non-local algorithm in this work.

III. MONTE CARLO RESULTS

In our Monte Carlo calculations, we use the standard Metropolis algorithm with periodic boundary conditions in both the $\hat{x}$ and $(\hat{x} + \sqrt{3}\hat{y})/2$ directions of a 50×50 triangular lattice.[44] This size lattice is comparable to the size of defect-free regions in the experimental system.[45] In particular, the steps on this surface have a spacing on this order. This size also allows easy visual inspection without undue finite-size effects, as well as affording reasonable computational costs. Specifically, we mostly take 100,000 MC steps per site through the entire lattice to equilibrate the system, after which we take an additional 250,000 MC steps to get the ground state of the system. Near the transition temperature, we use 5 times as many MC steps for equilibration and 4 times as many steps for averaging.

For the particle density ρ, we use mostly $\rho = 0.4$, sometimes $\rho = 0.3$ and $\rho = 0.33$. We usually set the temperature $T = 0.001\epsilon/k_B$, where ϵ is the unit energy of our system, but sometimes we vary T. For the attractions, we use $E_1 = 0.07\epsilon - A$, $E_{\rm LT} = 0.05\epsilon$, $E_{\rm IT} = 0.06\epsilon$, $E_6 = 0.06\epsilon$, E_{12}, and E_{19}. For the repulsions, we use mostly $E_{\rm T} = 0.06\epsilon$ (sometimes $E_{\rm T} = 0.03\epsilon$) and $A = 0.03\epsilon$, where we summed up to the $6th$ nearest-neighbors. Note that the signs are already included in the Hamiltonian (2), so these coefficients specify only the magnitudes of interactions.

When E_{19} attraction is used at $\rho = 0.4$, we get E_6 hexagons, three particles on a side, for several values of E_{19}, as in Fig. 3. $E_{19} = 0.06\epsilon$ has the most E_6 hexagons (116, 65.9%). When $\rho = 0.3$, $E_{19} = 0.08\epsilon$ there are E_{19} hexagons, five particles on a side, as shown in the inset to Fig. 3. However, for most values of E_{19} at $\rho = 0.4$ there are E_6 hexagons, but for particular values of E_{19} (such as $E_{19} = 0.08\epsilon$) with $\rho = 0.3$ there are E_{19} hexagons.

E_{12} attractions lead to E_{12} hexagons, with four particles on a side, for $0.03\epsilon \le E_{12} \le 0.12\epsilon$ with $E_{\rm T} = 0.06\epsilon$ and for $0.02\epsilon \le E_{12} \le 0.15\epsilon$ (but missing at some values such as 0.05ϵ, 0.12ϵ, and 0.14ϵ) with $E_{\rm T} = 0.03\epsilon$, when $\rho = 0.33$, and for $0.03\epsilon \le E_{12} \le 0.15\epsilon$ (except $E_{12} = 0.14\epsilon$) with $E_{\rm T} = 0.06\epsilon$ when $\rho = 0.4$ as illustrated in Fig. 4. $E_{12} = 0.11\epsilon$ leads to the most E_{12} hexagons, 45 (60.0%) with $E_{\rm T} = 0.06\epsilon$ and 41 (54.7%) with $E_{\rm T} = 0.03\epsilon$ when $\rho = 0.33$, 12 (16.0%)

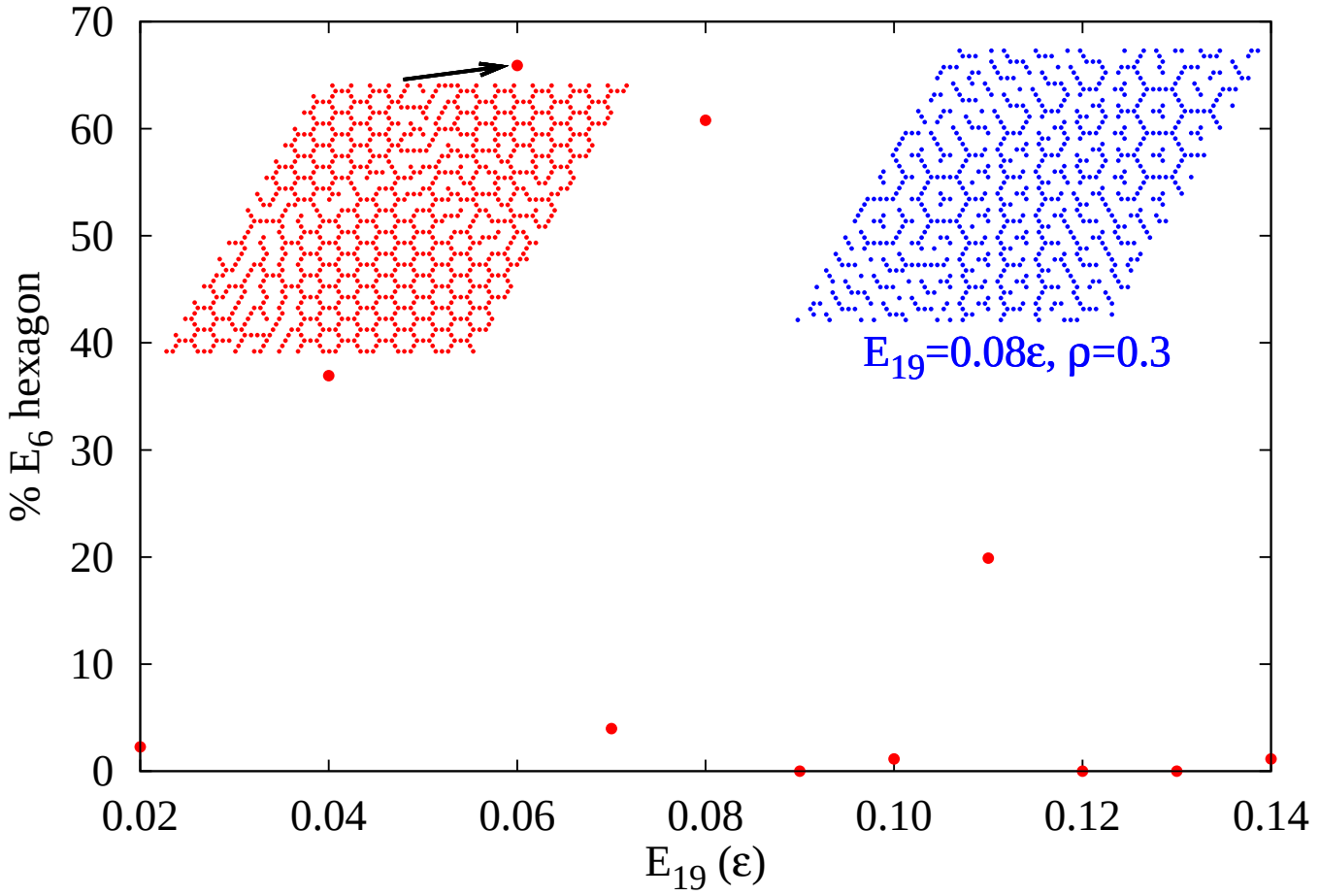

FIG. 3: (Color online) Percentage of E_6 hexagons as a function of the magnitude of E_{19} at $\rho = 0.4$. The ground state site configuration is also shown for $E_{19} = 0.06\epsilon$. The other ground state site configuration shown is for $E_{19} = 0.08\epsilon$, $\rho = 0.3$, where E_{19} hexagons form.

with $E_{\rm T} = 0.06\epsilon$ when $\rho = 0.4$. For $\rho = 0.4$ there are less E_{12} hexagons than for $\rho = 0.33$ overall. For $E_{12} = 0.11\epsilon$ with $E_{\rm T} = 0.06\epsilon$ and $\rho = 0.33$, there are long straight branches as well. Curiously, there is one particle at the center of each E_{12} hexagon, which seems to be a byproduct of this model.

When both E_{12} and E_{19} attractions are present, there are E_6 hexagons when $E_{12} < E_{19}$, e. g., for $E_{12} = 0.05\epsilon$, $E_{19} = 0.08\epsilon$, $\rho = 0.4$ with $E_{\rm T} = 0.06\epsilon$. Otherwise, there are E_{12} hexagons with combinations such as shown in Fig. 5. For $E_{12} = 0.06\epsilon$, $E_{19} = 0.03\epsilon$, $\rho = 0.33$ with $E_{\rm T} = 0.06\epsilon$, there are 73 (97.3%) E_{12} hexagons out of a possible 75, so near perfection. Overall, there are more E_{12} hexagons for $\rho = 0.33$ than for $\rho = 0.4$.

For E_6 attraction there are E_6 hexagons, as shown for $\rho = 0.4$ in Fig. 6 with E_6 ranging from 0.01ϵ to 0.10ϵ in increments of 0.01ϵ. More E_6 hexagons form at $E_6 = 0.05\epsilon$ or higher. $E_6 = 0.10\epsilon$, $\rho = 0.4$, $T = 0.001\epsilon/k_B$ makes 143 (81.3%) E_6 hexagons (out of a possible 176 E_6 hexagons), while for $E_6 = 0.06\epsilon$, $\rho = 0.4$, $T = 0.1\epsilon/k_B$, there are 141 (80.1%) E_6 hexagons. In contrast, when E_6 is taken as repulsive, only straight branches form, as shown for $E_6 = -0.06\epsilon$ and for $E_6 = -0.03\epsilon$ in Fig. 7. Therefore, the long-range repulsion seems inconsistent with the formation of a honeycomb structure.

When there are both E_6 and E_{19} attractions, E_6 hexagons form as shown in Fig. 8. With a fixed $E_6 = 0.06\epsilon$, there are a lot more E_6 hexagons for $\rho = 0.4$ than for $\rho = 0.3$. For $E_6 = 0.06\epsilon$, $E_{19} = 0.07\epsilon$, $\rho = 0.4$ there are 156 (88.6%) E_6 hexagons, in comparison to only 28 (15.9%) when $E_6 = 0.06\epsilon$, $E_{19} = 0.02$, $\rho = 0.3$. When E_6 repulsion is combined with E_{19} attraction, irregular shapes and long straight branches form, as verified for $E_6 = -0.03\epsilon$, $E_{19} = 0.06\epsilon$, $\rho = 0.4$ (not depicted).

When E_6 and E_{12} attractions are present, E_6 hexagons dominate, as seen in Figs. 9 and 10. E_6 is fixed at 0.06ϵ in Fig. 9 but is allowed to vary in Fig. 10. The latter is an extension of the former. In both figures, there are generally

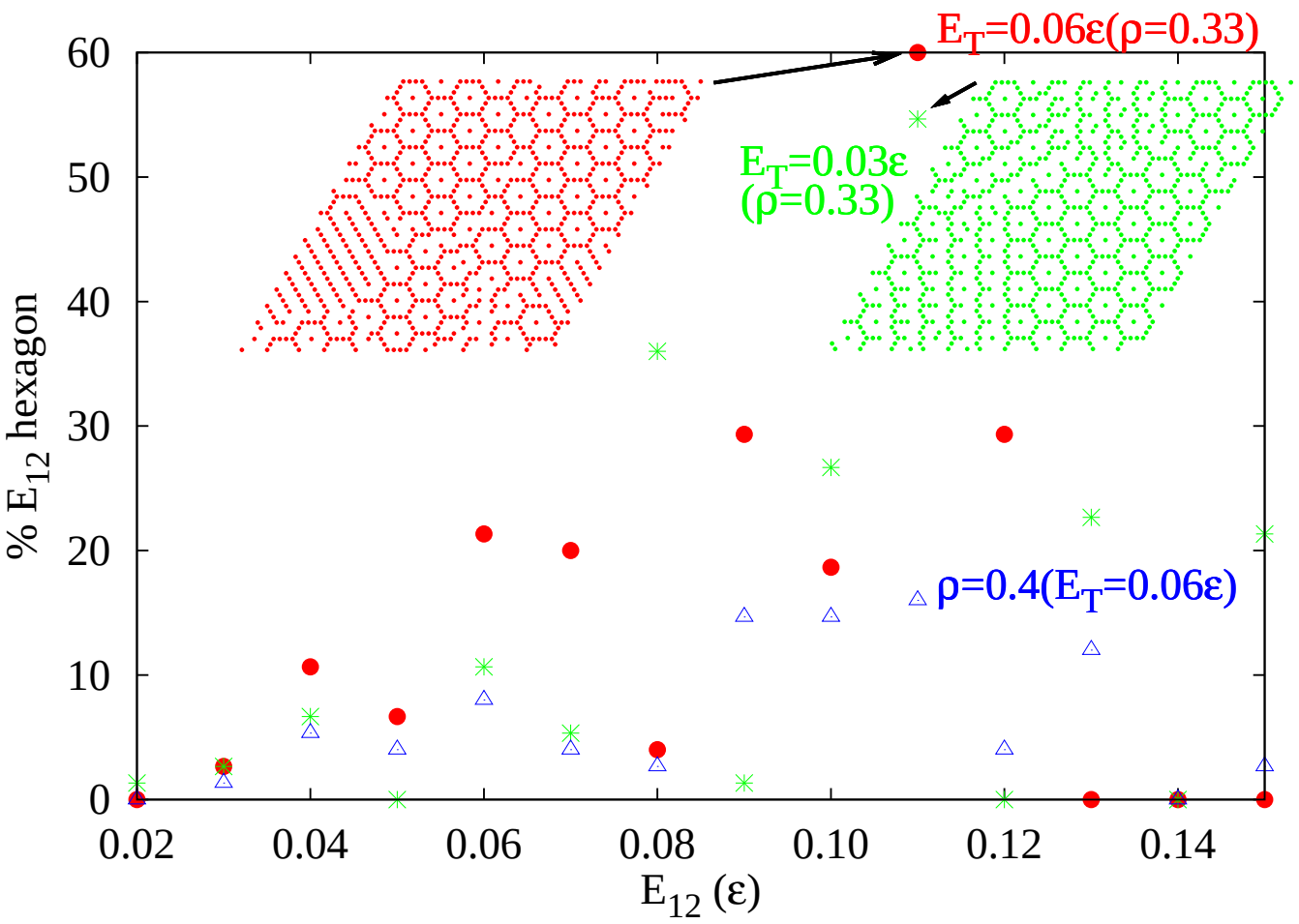

FIG. 4: (Color online) Percentage of E_{12} hexagons as a function of the magnitude of E_{12} at $\rho = 0.33$ with $E_{\rm T} = 0.06\epsilon$ and with $E_{\rm T} = 0.03\epsilon$, and at $\rho = 0.4$ with $E_{\rm T} = 0.06\epsilon$. The ground state site configurations are also shown at $E_{12} = 0.11\epsilon$, $\rho = 0.33$ with $E_{\rm T} = 0.06\epsilon$ and with $E_{\rm T} = 0.03\epsilon$.

more E_6 hexagons for $\rho = 0.4$ than for $\rho = 0.33$. Moreover, long straight branches as well as E_6 hexagons are observed at $E_6 = 0.04\epsilon$, $E_{12} = 0.01\epsilon$, $\rho = 0.33$ whereas both E_6 and E_{12} hexagons are observed at $E_6 = 0.03\epsilon$, $E_{12} = 0.03\epsilon$, $\rho = 0.33$.

When E_6, E_{12}, and E_{19} attractions are all present, only E_6 hexagons form with $\rho = 0.33$ or $\rho = 0.4$ as in Table I. The ground state site configurations for the two cases $E_6 = E_{12} = E_{19} = 0.06\epsilon$, $\rho = 0.4$; $E_6 = E_{12} = E_{19} = 0.03\epsilon$, $\rho = 0.4$ are shown in Fig. 11. The former makes the most (160, 90.9%) E_6 hexagons throughout this work. There are generally more E_6 hexagons for $\rho = 0.4$ than for $\rho = 0.33$. Even when E_{12} and E_{19} repulsions in the dipolar repulsion term are included to these combinations, little differences are observed due to negligible contributions from these repulsions in the A term because of R^{-3} factor. These three-parameter combinations work fine when the interaction strength is not too large altogether or gradually decreases with distance as expected. When $E_{\rm T} = 0.03\epsilon$, it also works well even though there are generally fewer E_6 hexagons than when $E_{\rm T} = 0.06\epsilon$.

Next we try different values of $E_{\rm LT}$ and $E_{\rm IT}$, as shown in Fig. 12. They all work well as long as $E_{\rm LT}$ and $E_{\rm IT}$ are not small at the same time. Also there are a lot more E_6 hexagons for $\rho = 0.4$ than for $\rho = 0.3$. For $E_{\rm LT} = E_{\rm IT} = 0.05\epsilon$, $\rho = 0.4$ and $E_{\rm LT} = E_{\rm IT} = 0.04\epsilon$, $\rho = 0.4$ there are the same number, 128 (72.7%) of E_6 hexagons while for $E_{\rm LT} = 0.06\epsilon$, $E_{\rm IT} = 0.03\epsilon$, $\rho = 0.3$ there are just 67 (38.1%) E_6 hexagons.

For different values of A, such as from $A = 0.01\epsilon$ to $A = 0.08\epsilon$ with the increment of 0.01ϵ when $\rho = 0.33$ or $\rho = 0.4$, all work fine as long as A is in the range of reasonable strength as in Fig. 13. There are a lot more E_6 hexagons for $\rho = 0.4$ than for $\rho = 0.33$. For $A = 0.02\epsilon$, $\rho = 0.33$ leads to 35 (19.9%) E_6 hexagons, in comparison to 143 (81.3%) for $A = 0.08\epsilon$, $\rho = 0.4$.

To consolidate these findings for the coupling constants, we draw a Venn diagram in Fig. 14 to show which components are necessary to make which hexagons. Typically, E_1, $E_{\rm LT}$, $E_{\rm IT}$ attractions and A, $E_{\rm T}$ repulsions are needed.

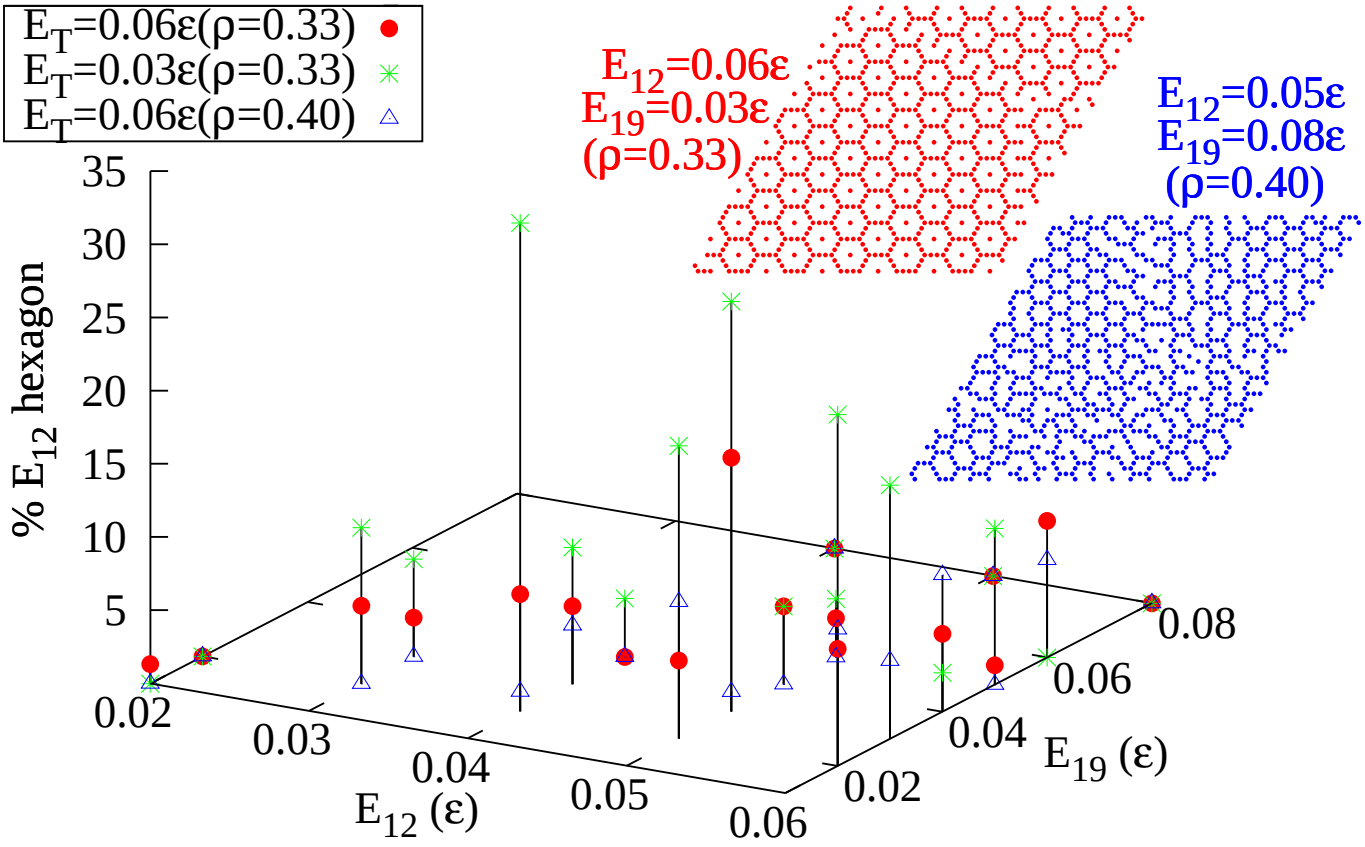

FIG. 5: (Color online) Percentage of E_{12} hexagons as a function of the magnitudes of E_{12} and E_{19} at $\rho = 0.33$ with $E_{\rm T} = 0.06\epsilon$ and with $E_{\rm T} = 0.03\epsilon$, and at $\rho = 0.40$ with $E_{\rm T} = 0.06\epsilon$. The ground state site configuration is shown at $E_{12} = 0.06\epsilon$, $E_{19} = 0.03\epsilon$, $\rho = 0.33$ with $E_{\rm T} = 0.06\epsilon$, of which data point (73 E_{12} hexagons, 97.3%) is not shown in the percentage plot since it is too big compared to the others. The other ground state site configuration is at $E_{12} = 0.05\epsilon$, $E_{19} = 0.08\epsilon$, $\rho = 0.40$ with $E_{\rm T} = 0.06\epsilon$, where E_6 hexagons form instead of E_{12}.

For clarity the repulsions are denoted with a negative sign. The diagram also shows which hexagons form when two or three long-range attractions are combined together. When there are both E_6 and E_{12} attractions, E_6 hexagons occur mostly, but in some cases both E_6 and E_{12} hexagons appear. When there are both E_6 and E_{19} attractions, only E_6 hexagons arise. When both E_{12} and E_{19} attractions are present, E_{12} hexagons occur mostly, but in some cases there are E_6 hexagons instead. The presence of all three E_6, E_{12}, and E_{19} attractions leads to only E_6 hexagons. In contrast, E_6 repulsion leads to only straight branches.

In Fig. 15 we show the effect of varying the temperature when $\rho = 0.4$. Here each point is an average over 100 different runs. The ground state site configurations are also shown at the temperatures $T = 0.1\epsilon/k_B$, $T = 0.495\epsilon/k_B$, and $T = 0.7\epsilon/k_B$. The honeycomb structure breaks down at $T_c = 0.495\epsilon/k_B$, which is a transition temperature.

Finally, we see the particle density change at $T = 0.001\epsilon/k_B$ in Fig. 16. Here also each point is an average over 100 different runs. Experimentally it is observed that there are 18 AQ molecules on top of 444 Cu substrate atoms. In our system there are 12 occupied sites out of 19 sites. Since we are mapping one AQ molecule to one occupied site, there must be some equivalence between these two as $18/444 = 12/296 \equiv 12/19$. From here we can derive a conversion factor as $f = 296/19 = 15.579$. Experimentally it is claimed that the honeycomb structure starts to appear at the local coverage of 15 AQ molecules per 1000 substrate Cu atoms, thus, using this conversion factor, $15/1000 \equiv 15/64.189 = 0.234$ in our system. Also Fig. 3 of Ref. 14 shows a honeycomb structure up to 35 AQ molecules per 1000 substrate atoms, which is $35/1000 \equiv 35/64.189 = 0.545$ in our system. Therefore it would be useful to look into the particle density change from $\rho = 0.23$ to $\rho = 0.55$ in our system. Unlike the prediction, hexagons start to appear at $\rho = 0.3$ in our system. However the honeycomb structure remains up to $\rho = 0.55$. As

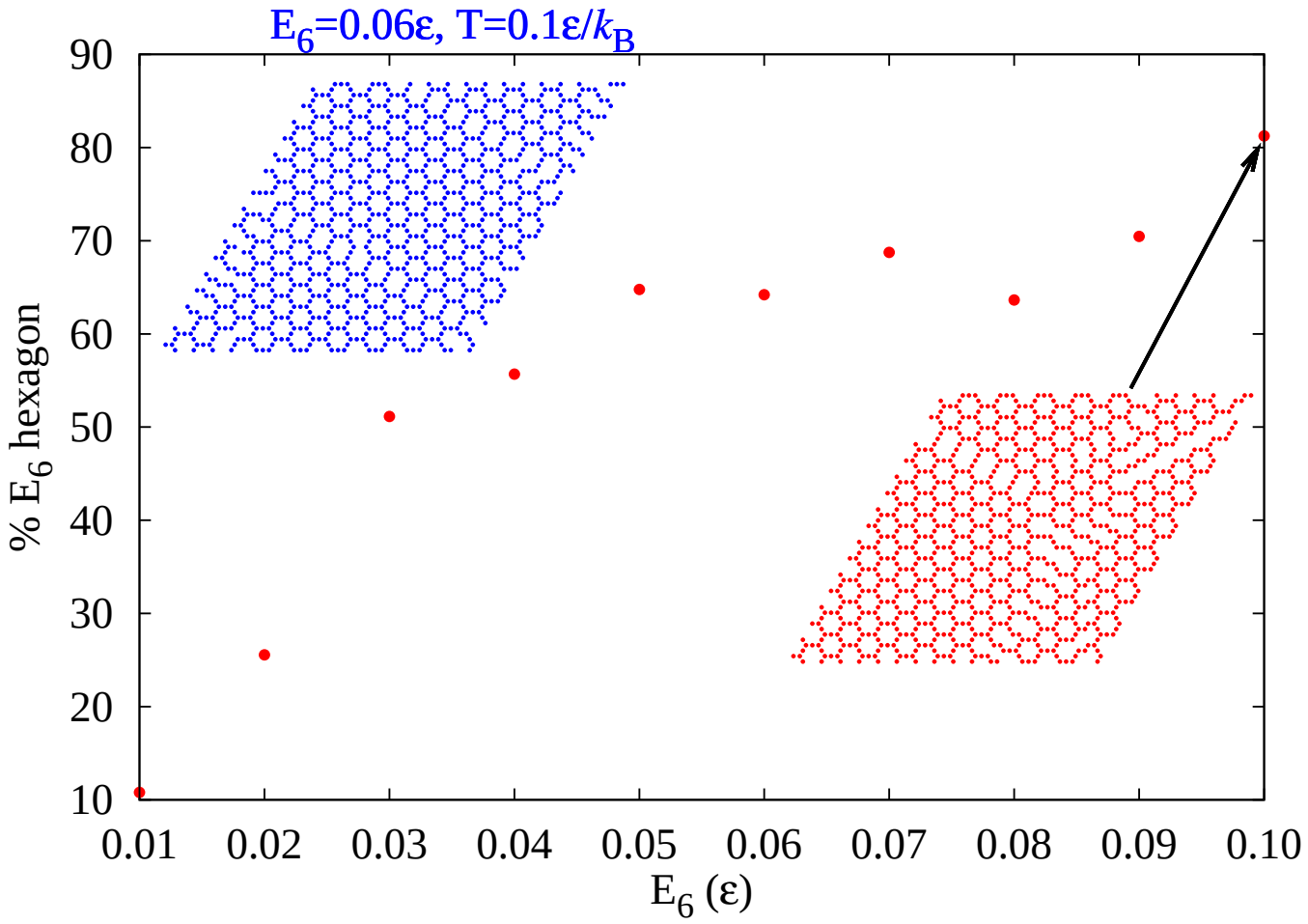

FIG. 6: (Color online) Percentage of E_6 hexagons as a function of the magnitude of E_6 at $\rho = 0.4$ ($T = 0.001\epsilon/k_B$). The ground state site configuration is also shown at $E_6 = 0.10\epsilon$, which makes 143 (81.3%) E_6 hexagons. The other ground state site configuration shown is at $E_6 = 0.06\epsilon$, $\rho = 0.4$, $T = 0.1\epsilon/k_B$, where also many E_6 hexagons (141, 80.1%) form.

ρ increases, the percentage of E_6 hexagons reaches a maximum around 0.4 and then decreases slightly as clustered domains appear. This slight decrease of hexagons is in contrast to the plateau in the experimental histogram around 35/1000 (cf. Fig. 3 of Ref. 14). We think this is due to the finite size effect of our system since 12 out of 19 is too large compared to 18 out of 444. Other than this, our results generally agree well with the experimental observations.

IV. DISCUSSION & CONCLUSIONS

In this paper, we have simulated the spontaneous formation of honeycomb structures of AQ molecules on a Cu(111) surface in terms of a simple lattice gas model. Within this model, we find that long-range attractive interactions are necessary to make honeycomb structures, a scenario that differs from the predictions of Ref. 14. Among these attractions, the E_6 attraction is the most important to the formation of honeycomb structures. The addition of E_{12} and/or E_{19} attractions to the E_6 attraction enhances the formation of E_6 hexagons. When there are only E_{12} and/or E_{19} attractions, larger hexagons and longer straight branches form. When E_6 is repulsive, only straight branches form. The trio repulsion E_{T} (or some equivalent) is crucial to prevent compact, dense clusters. Varying temperature at $\rho = 0.4$, we find the transition temperature $T_c = 0.495\epsilon/k_B$. Varying the particle density at $T = 0.001\epsilon/k_B$, we find that the honeycomb structure starts to form at $\rho = 0.3$, peaks at $\rho = 0.4$, and exists up to $\rho = 0.55$, with a slight decrease of the number of E_6 hexagons after the peak.

One of the benefits of using this kind of simplified model is that we can reduce a complicated system into a system of manageable size. A system such as ours, which cannot be understood with any high-level methods or would demand an

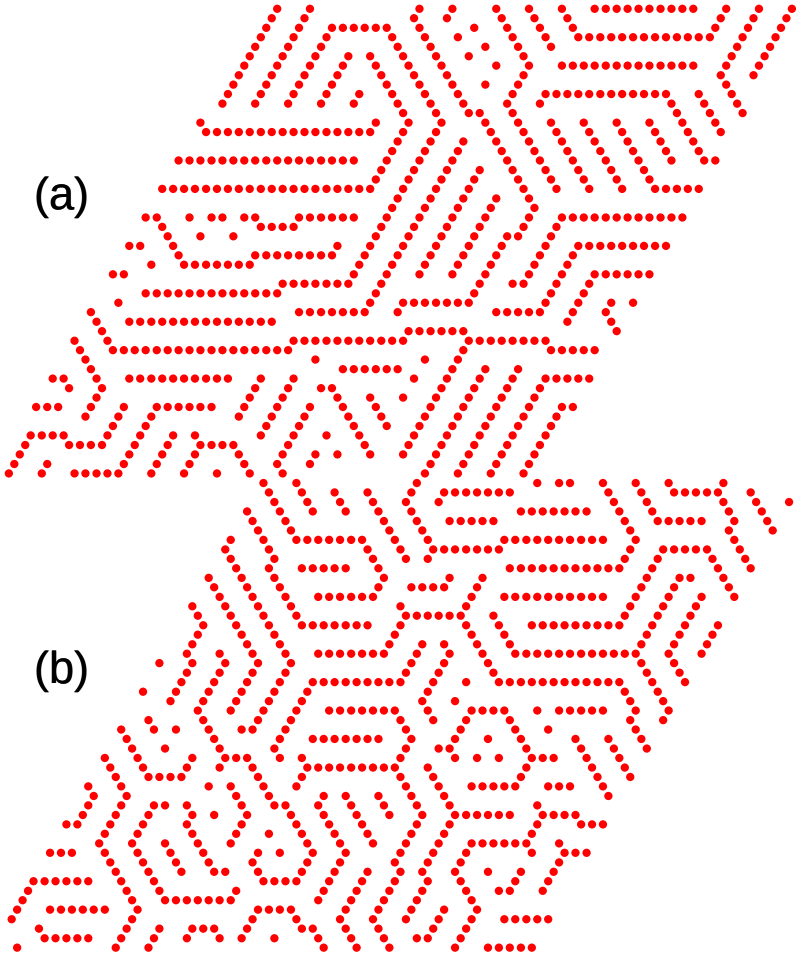

FIG. 7: (Color online) The ground state site configurations for E_6 repulsions of (a) $E_6 = -0.06\epsilon$ and (b) $E_6 = -0.03\epsilon$. Only straight branches form.

enormous amount of computing power as it is, can be at least approached with this kind of model. Another benefit is that we can get a global accounting of the given system with the introduction of just a few basic interaction parameters. These basic interaction parameters can be easily replaced with others when they do not reproduce the ordering. The complicated mechanism of the system can be easily understood with minimal interactions. A shortcoming of our model is that we cannot probe the detailed mechanism at work at the atomic level since the complicated system is simplified by grouping many atoms into one entity. Since some degrees of freedom of individual atoms are lost in the simplification process, it is necessary to consider whether these losses affect the overall mechanism of the whole system before adopting this kind of procedure.

There could be other possible choices of combinations of coupling constants, or even completely different coupling parameters, than used in this work to simulate the formation of honeycomb structures. However, within the type and range of coupling parameters in our investigation, the results given in this work are the best of our knowledge as long as the unit energy is kept constant as in this work. Most notably, our calculations provide strong evidence that the long-range attractive interactions are important (this does not mean that the short-range interactions are not necessary. They are assumed to be already included.) to explain the spontaneous formation of AQ's honeycomb structure.

We could compare the percentage of E_6 hexagons as a function of the particle density ρ with the experimental observation as in Ref. 14 but had no way to compare our transition temperature $T_c = 0.495\epsilon/k_B$ at $\rho = 0.4$ with a corresponding experimental observation since the value of our unit energy ϵ was not known. Ref. 14 reports observations of the spontaneous formation of honeycomb structures between 10 and 200 K, To obtain an estimate of ϵ, we suppose that T_c is 200 K; then $\epsilon \approx 35$ meV, so much less than the crude estimate of E_1 noted after Eq. (2). The actual value might turn out to be somewhat larger, but in any case the long-range attractions are then of order just

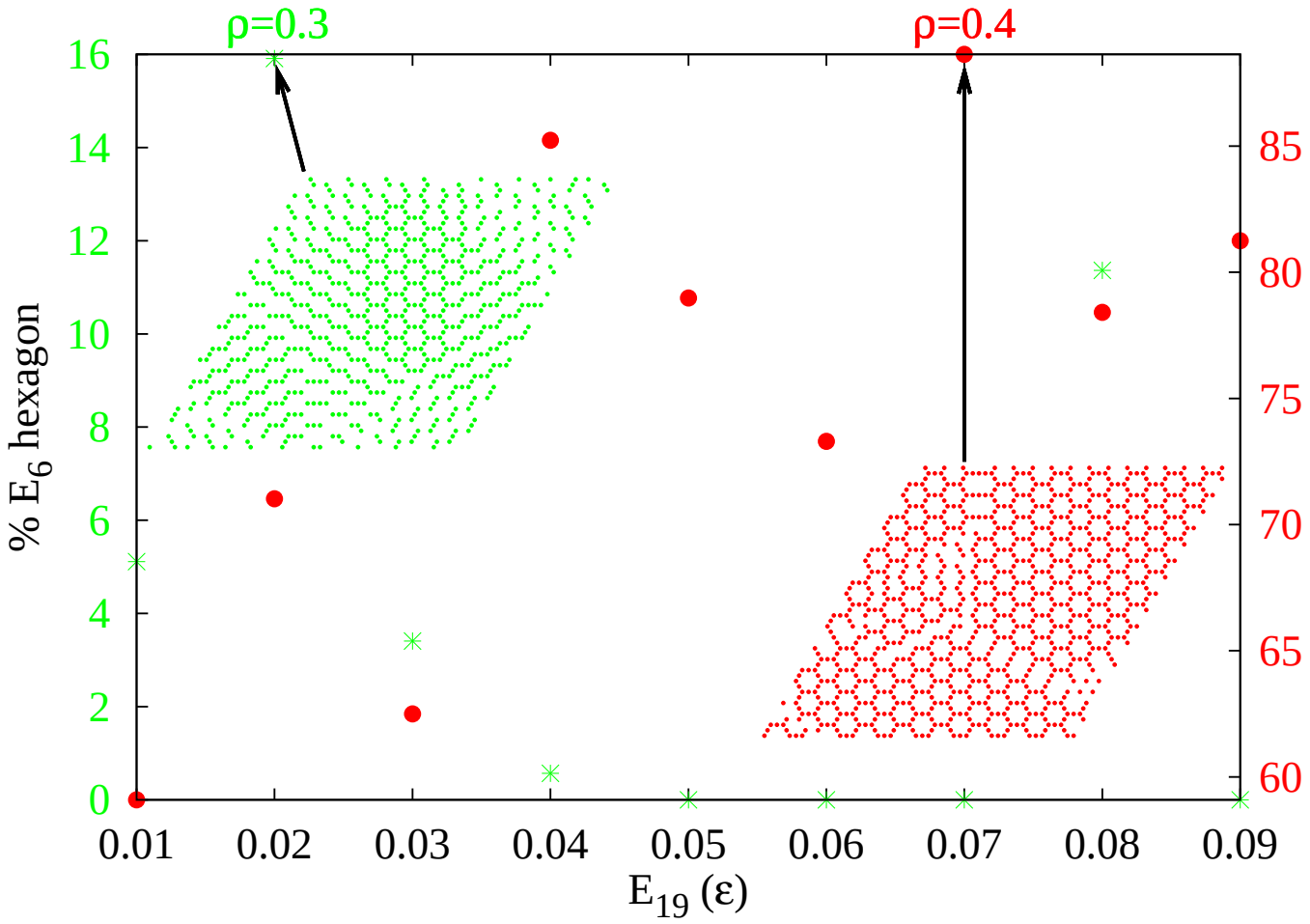

FIG. 8: (Color online) Percentage of E_6 hexagons as a function of the magnitude of E_{19} with a fixed $E_6 = 0.06\epsilon$ at $\rho = 0.3$ (green asterisks) and at $\rho = 0.4$ (red solid circles). $E_T = 0.06\epsilon$ for both cases. The solid circles are scaled to the right axis while the asterisks to the left. The ground state site configurations are shown at $E_6 = 0.06\epsilon$, $E_{19} = 0.02\epsilon$, $\rho = 0.3$ and at $E_6 = 0.06\epsilon$, $E_{19} = 0.07\epsilon$, $\rho = 0.4$, where there are 28 (15.9%) and 156 (88.6%) E_6 hexagons, respectively. There are a lot more E_6 hexagons for $\rho = 0.4$ than for $\rho = 0.3$.

a couple meV, consistent with an interaction mediated by the metallic surface state of Cu(111).

Our mapping of one AQ molecule onto one occupied site (done to make our simulations manageable) assumes one occupied site at a vertex of a hexagon; this is a simplification of the actual experimental system since *three* AQ molecules form a vertex of a hexagon as a pinwheel shape. Therefore it is not clear whether it is more appropriate to say that there are three or four molecules on a side of a hexagon. Our E_6 hexagon invariably has three occupied sites on a side while our E_{12} hexagon has four on a side. While the actual AQ hexagon is midway between our E_6 and E_{12} hexagons, we assumed it is closer to the E_6 hexagon since only one configuration of the pinwheel shape was experimentally observed in a domain. This is also one reason why we introduced the trio repulsion to our model. It is likely that the neglected degrees of freedom of the internal structure of the AQ molecule in our simplified model affect the coverage at which compact clumped clusters appear at high ρ in our simulations (cf. $\rho = 0.55$ in Fig. 16); while not reported in Ref. 14, dense regions do occur experimentally at high enough coverages. To include all the internal degrees of freedom of the AQ molecule, we would have to turn to large-scale molecular dynamics, which is beyond the scope of our investigation. Since our model does not specify that the adsorbed molecule be an AQ, it can serve as a possible framework for analyzing experiments involving different adsorbates.

While we did not go beyond the lattice gas model regarding the role of a substrate on the formation of a honeycomb structure of adsorbed AQ molecules, this effect is already included implicitly in the variables of the long-range attractions and the dipolar repulsions, since the origin of the long-range attractions is the indirect interaction mediated by metallic (partially occupied) surface states and the elastic and electrostatic dipoles depend on local relaxations. Thus, if we replace the current substrate with another substrate (e. g., Ag(111)), we would need to adjust all the

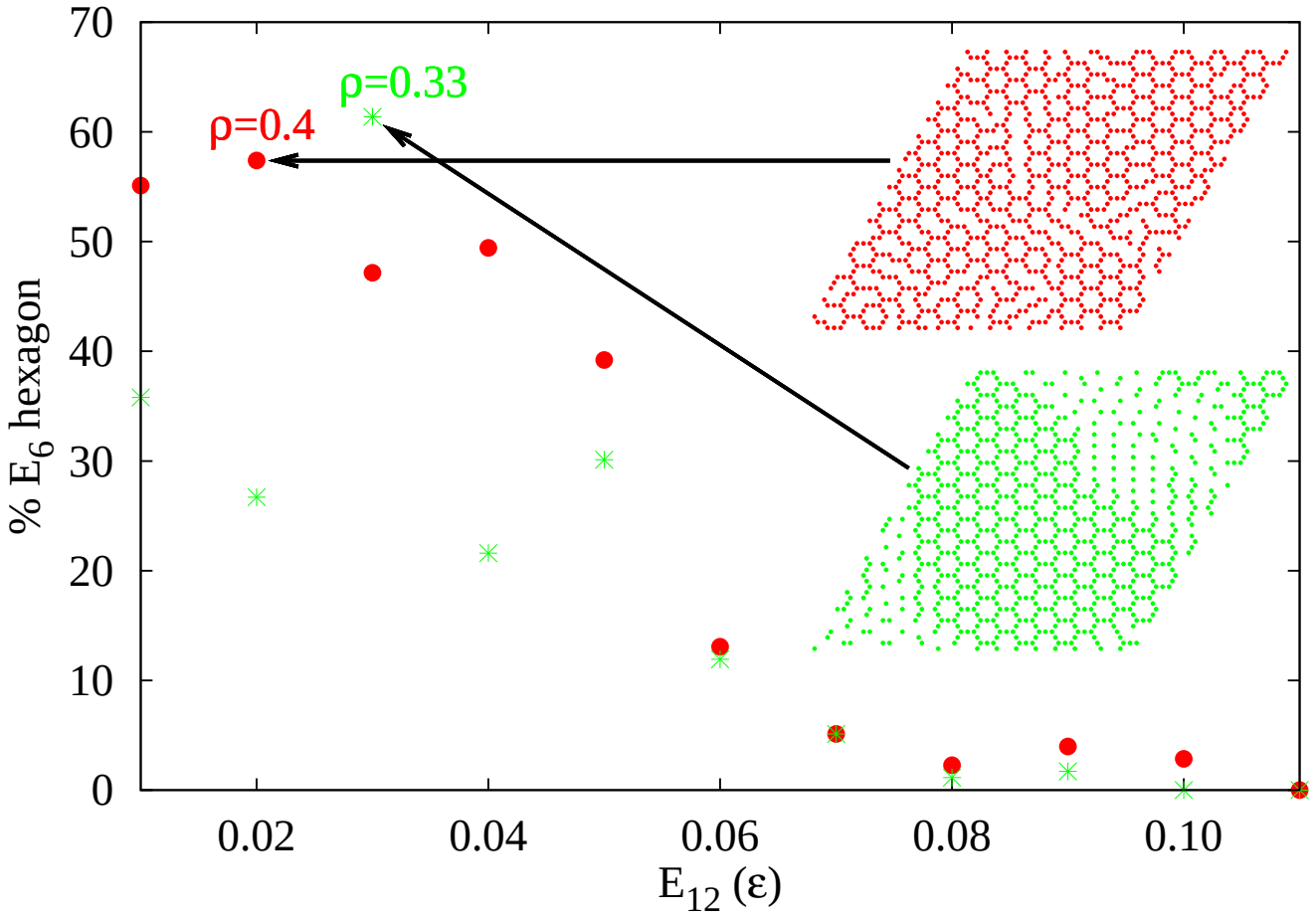

FIG. 9: (Color online) Percentage of E_6 hexagons as a function of the magnitude of E_{12} with a fixed $E_6 = 0.06\epsilon$ at $\rho = 0.33$ (green asterisks) and at $\rho = 0.4$ (red solid circles). $E_{\rm T} = 0.06\epsilon$ for both cases. The ground state site configurations are shown at $E_6 = 0.06\epsilon$, $E_{12} = 0.03\epsilon$, $\rho = 0.33$ and at $E_6 = 0.06\epsilon$, $E_{19} = 0.02\epsilon$, $\rho = 0.4$, where there are 108 (61.4%) and 101 (57.4%) E_6 hexagons, respectively. Generally there are more E_6 hexagons for $\rho = 0.4$ than for $\rho = 0.33$.

values of long-range attractions and dipolar repulsions accordingly.

Our choice of a 50×50 lattice throughout this work stems from the report Ref. 14 that the total number of hexagons in the scanning tunneling microscopy images is under 150 due to lattice defects, notably steps. With our lattice size, the perfect number of E_6 hexagons can be 176, which is more than enough to accommodate 150 hexagons. Moreover, our primary objective was to see whether our simplified model could produce a honeycomb structure spontaneously, not to try to extrapolate to the thermodynamic limit by using lattices much larger than the defect-free regions in the experiments. A 50×50 lattice is large enough to hold enough hexagons without introducing spurious finite-size effects. In addition, the computational cost of dealing with the lattice size of 50×50 was reasonable except for Figs. 15 and 16, where each point is an average over 100 different runs, costing much more than the other calculations. Even so, the overall computing cost was generally reasonable.

The ground-state image of the site configuration of each case is that of a particular run. Another run would produce a slightly different site configuration. Since we are not looking into the average value of a thermodynamic variable in these cases, it is not problematic to inspect just a single run. When we needed thermodynamic averages of many different runs, as in Figs. 15 and 16, we did perform many runs. Even in these many different runs, taking thermodynamic averages of different site configurations is not meaningful.

In summary, we have simulated the spontaneous formation of honeycomb structures of AQ molecules on a Cu(111) surface with the lattice gas model and MC calculations, identifying which long-range interactions are significant. In future work we will study the statistical mechanics and finite-size-limited phases of CO molecules confined within a hexagon of AQ molecules.

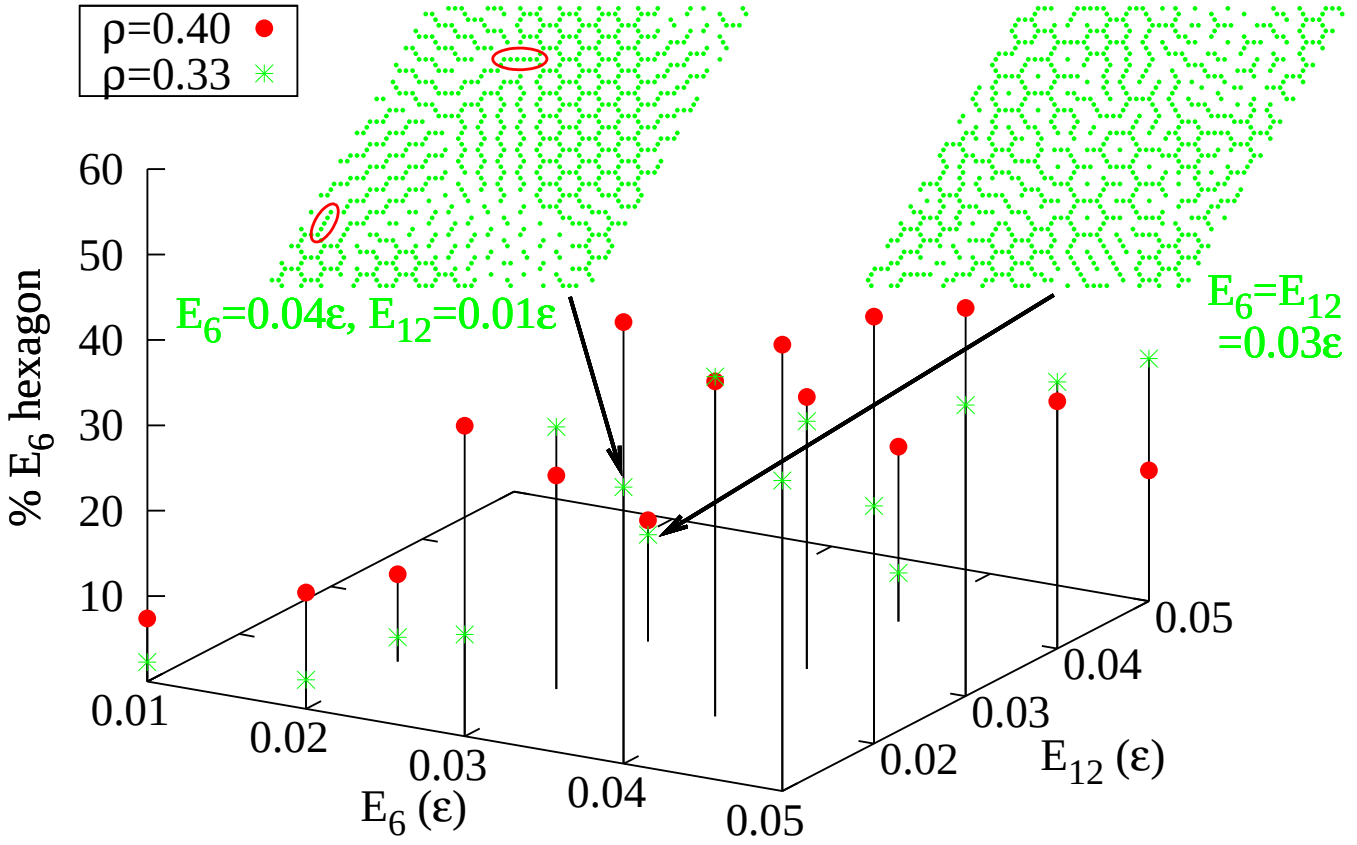

FIG. 10: (Color online) Percentage of E_6 hexagons as a function of the magnitudes of E_6 and E_{12} at $\rho = 0.33$ (green asterisks) and at $\rho = 0.4$ (red solid circles). $E_{\rm T} = 0.06\epsilon$ for both cases. The ground state site configurations are shown at $E_6 = 0.04\epsilon$, $E_{12} = 0.01\epsilon$, $\rho = 0.33$ and at $E_6 = 0.03\epsilon$, $E_{12} = 0.03\epsilon$, $\rho = 0.33$. For the former there are E_6 hexagons and long straight branches (marked with red ovals) while for the latter both E_6 and E_{12} hexagons are present. Here also there are generally more E_6 hexagons for $\rho = 0.4$ than for $\rho = 0.33$.

Acknowledgments

This work was supported primarily by NSF Grant CHE 07-50334, with secondary support from the Maryland MRSEC under NSF Grant DMR 05-20471 and ancillary support from the Center for Nanophysics and Advanced Materials (CNAM). We are grateful to John A. Tossell for assistance with the quantum chemical rough calculation of AQ interactions and to Ludwig Bartels and his group for helpful interactions and collaboration.

TABLE I: Combinations of E_6, E_{12}, and E_{19} which make E_6 hexagons. For $\rho = 0.4$ there are generally more E_6 hexagons than for $\rho = 0.33$. We found the most (160, 90.9%) E_6 hexagons for $E_6 = E_{12} = E_{19} = 0.06\epsilon$, $\rho = 0.4$ (see Fig. 11).

$E_6(\epsilon)$	$E_{12}(\epsilon)$	$E_{19}(\epsilon)$	ρ	# E_6 hexagons
0.06	0.06	0.06	0.33	69
			0.40	160
0.06	0.03	0.01	0.33	81
			0.40	119
0.03	0.03	0.03	0.33	84
			0.40	140
0.03	0.02	0.01	0.33	84
			0.40	128
0.05	0.05	0.05	0.33	76
			0.40	108
0.04	0.04	0.04	0.33	84
			0.40	98
0.02	0.02	0.02	0.33	88
			0.40	121
0.06	0.05	0.04	0.33	109
			0.40	105
0.06	0.04	0.02	0.33	109
			0.40	103
0.05	0.04	0.03	0.33	72
			0.40	101
0.04	0.03	0.02	0.33	113
			0.40	120

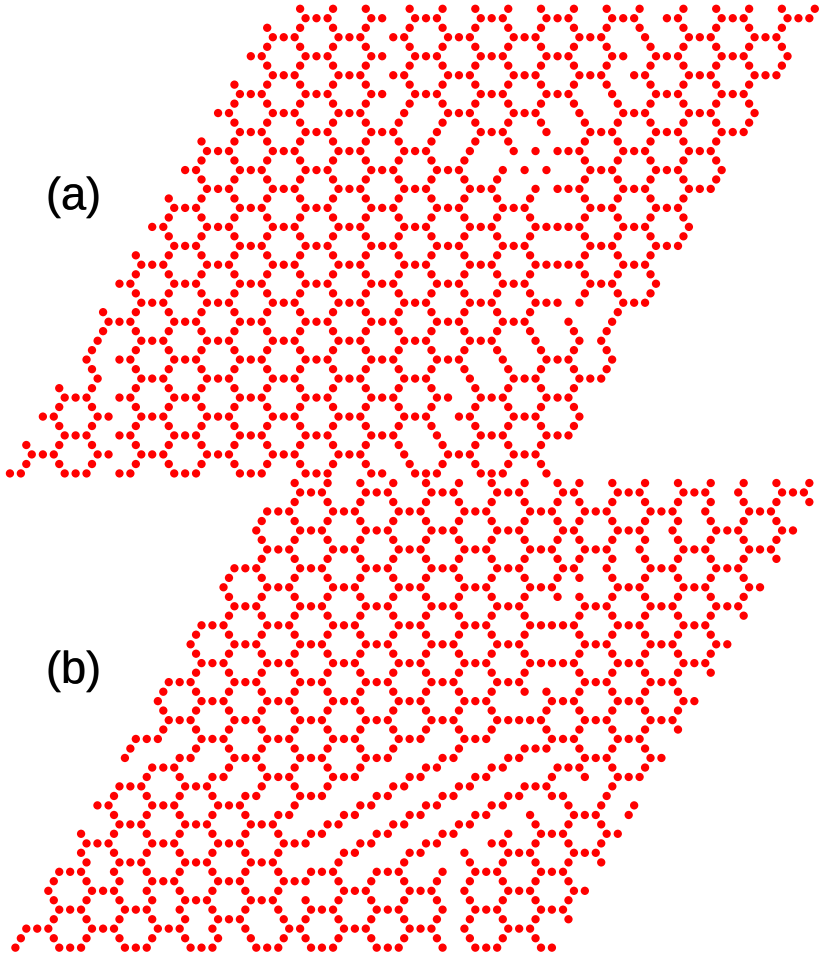

FIG. 11: (Color online) The ground state site configurations for (a) $E_6 = E_{12} = E_{19} = 0.06\epsilon$ and (b) $E_6 = E_{12} = E_{19} = 0.03\epsilon$. $\rho = 0.4$ for both cases. For the former there are 160 (90.9%) E_6 hexagons, the most in our investigation.

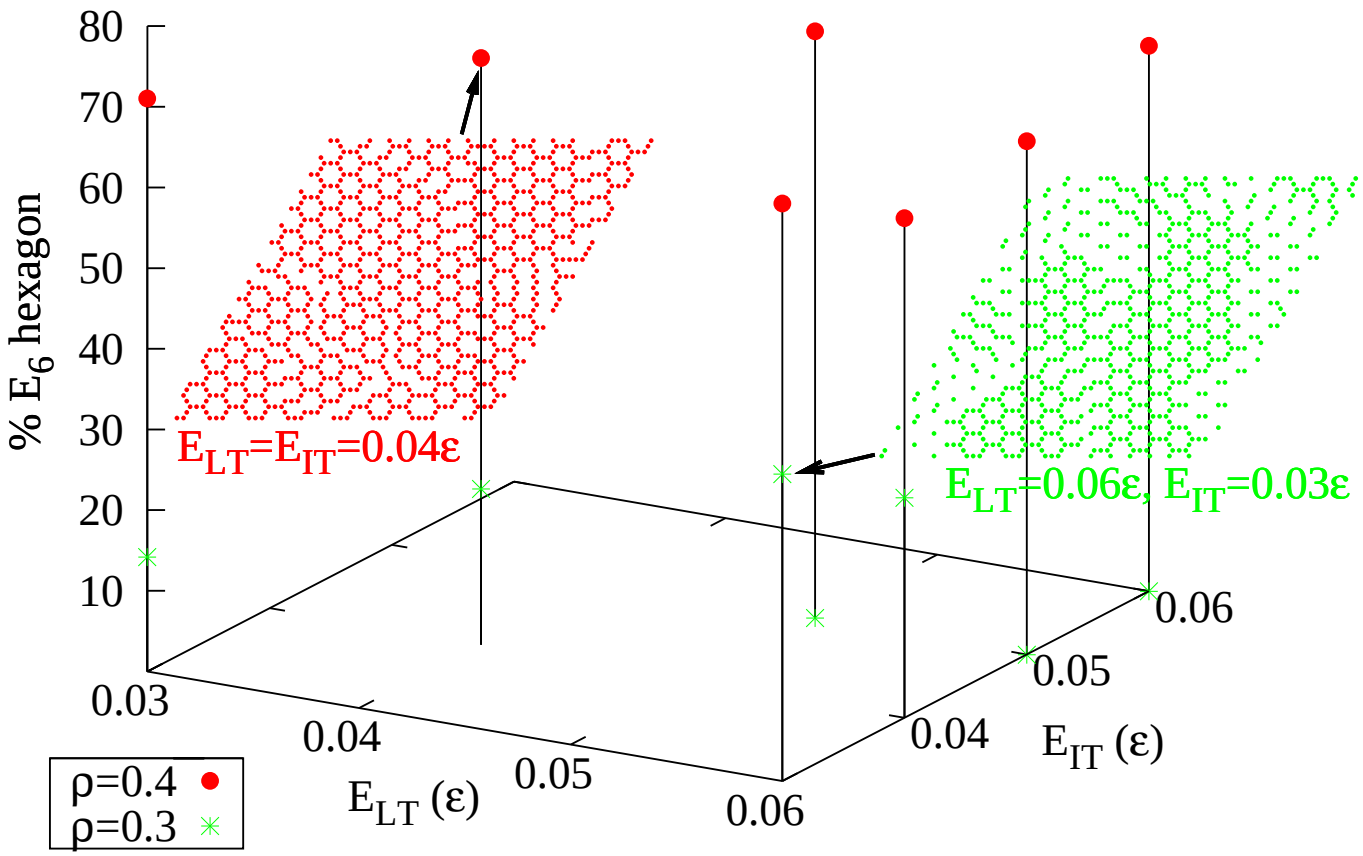

FIG. 12: (Color online) Percentage of E_6 hexagons as a function of the magnitudes of $E_{\rm LT}$ and $E_{\rm IT}$ at $\rho = 0.3$ (green asterisks) and at $\rho = 0.4$ (red solid circles). $E_{\rm T} = 0.06\epsilon$ for both cases. The ground state site configurations are shown at $E_{\rm LT} = 0.04\epsilon$, $E_{\rm IT} = 0.04\epsilon$, $\rho = 0.4$ and at $E_{\rm LT} = 0.06\epsilon$, $E_{\rm IT} = 0.03\epsilon$, $\rho = 0.3$. For the former and $E_{\rm LT} = 0.05\epsilon$, $E_{\rm IT} = 0.05\epsilon$, $\rho = 0.4$, there are the same 128 (72.7%) E_6 hexagons, while for the latter there are 67 (38.1%) E_6 hexagons. Obviously, there are more E_6 hexagons for $\rho = 0.4$ than for $\rho = 0.3$.

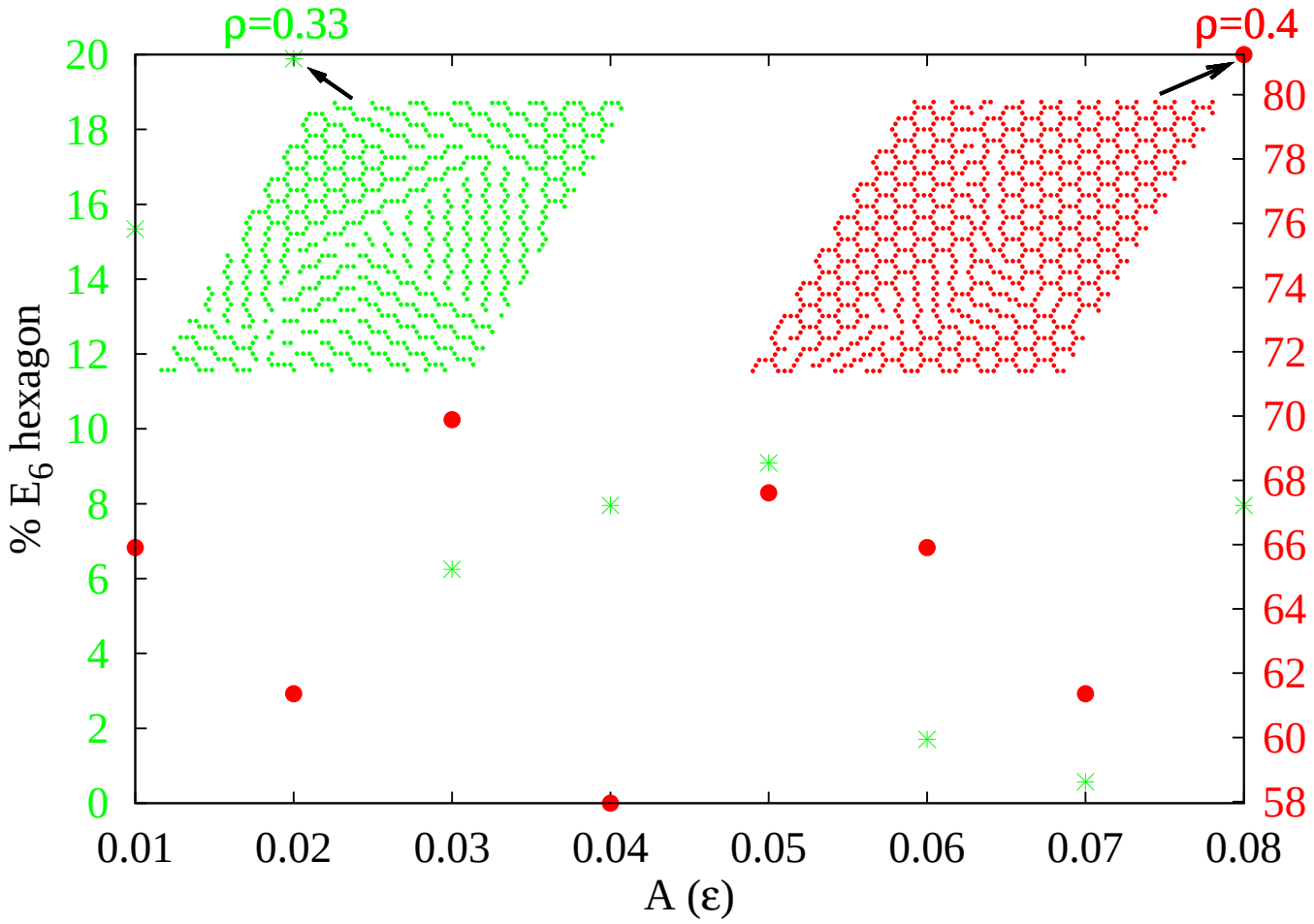

FIG. 13: (Color online) Percentage of E_6 hexagons as a function of the magnitude of A with a fixed $E_6 = 0.06\epsilon$ at $\rho = 0.33$ (green asterisks) and at $\rho = 0.4$ (red solid circles). $E_{\rm T} = 0.06\epsilon$ for both cases. The solid circles are scaled to the right axis while the asterisks to the left. The ground state site configurations are shown at $A = 0.02\epsilon$, $\rho = 0.33$ and at $A = 0.08\epsilon$, $\rho = 0.4$, for which there are 35 (19.9%) and 143 (81.3%) E_6 hexagons, respectively. There are many more E_6 hexagons for $\rho = 0.4$ than for $\rho = 0.33$.

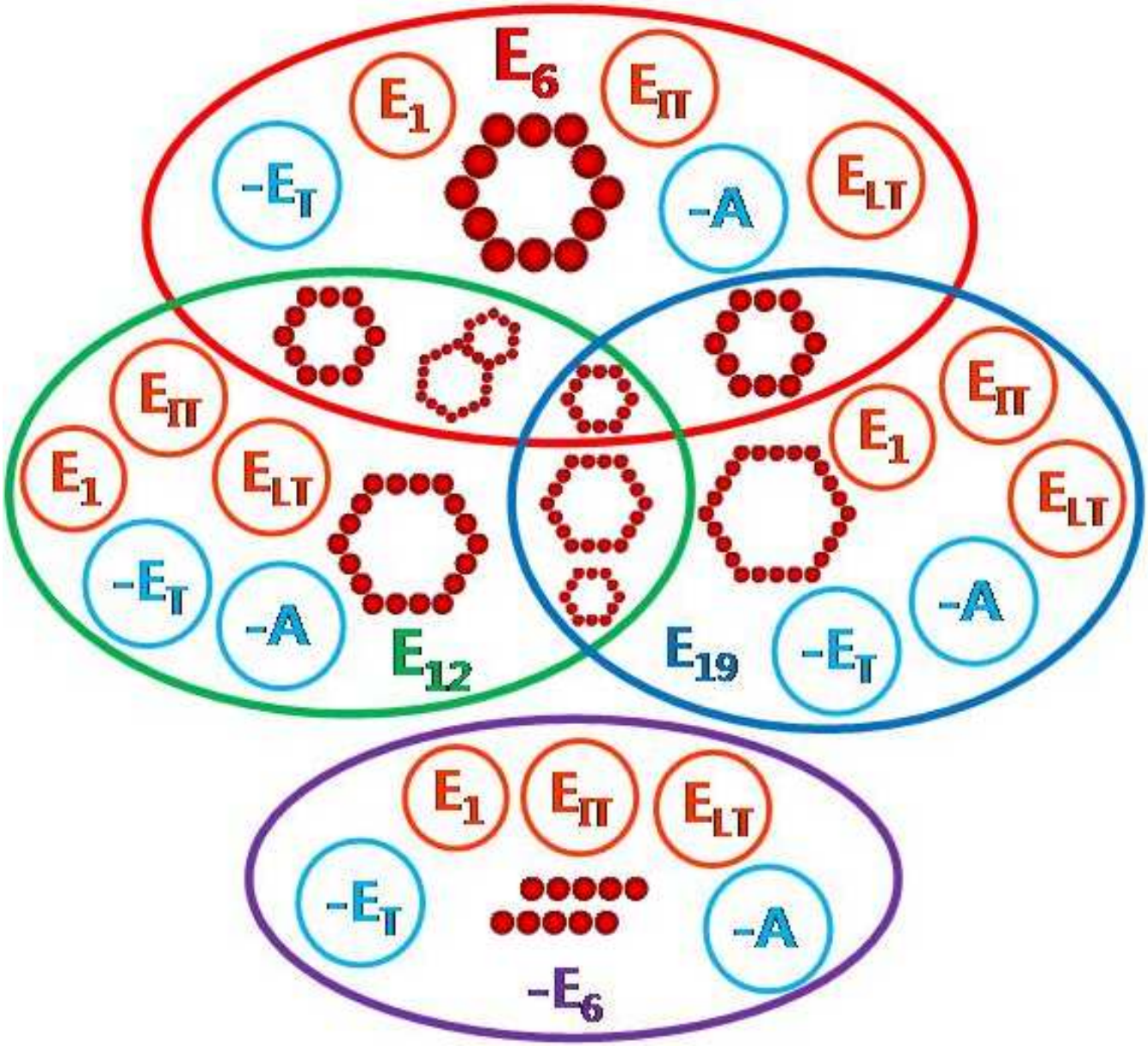

FIG. 14: (Color online) Venn diagram of coupling constants summing up all of our results. Which components are necessary to make which hexagons. Also which hexagons form when two or three long-range attractions are present at the same time. For clarity the repulsions are denoted with a negative sign.

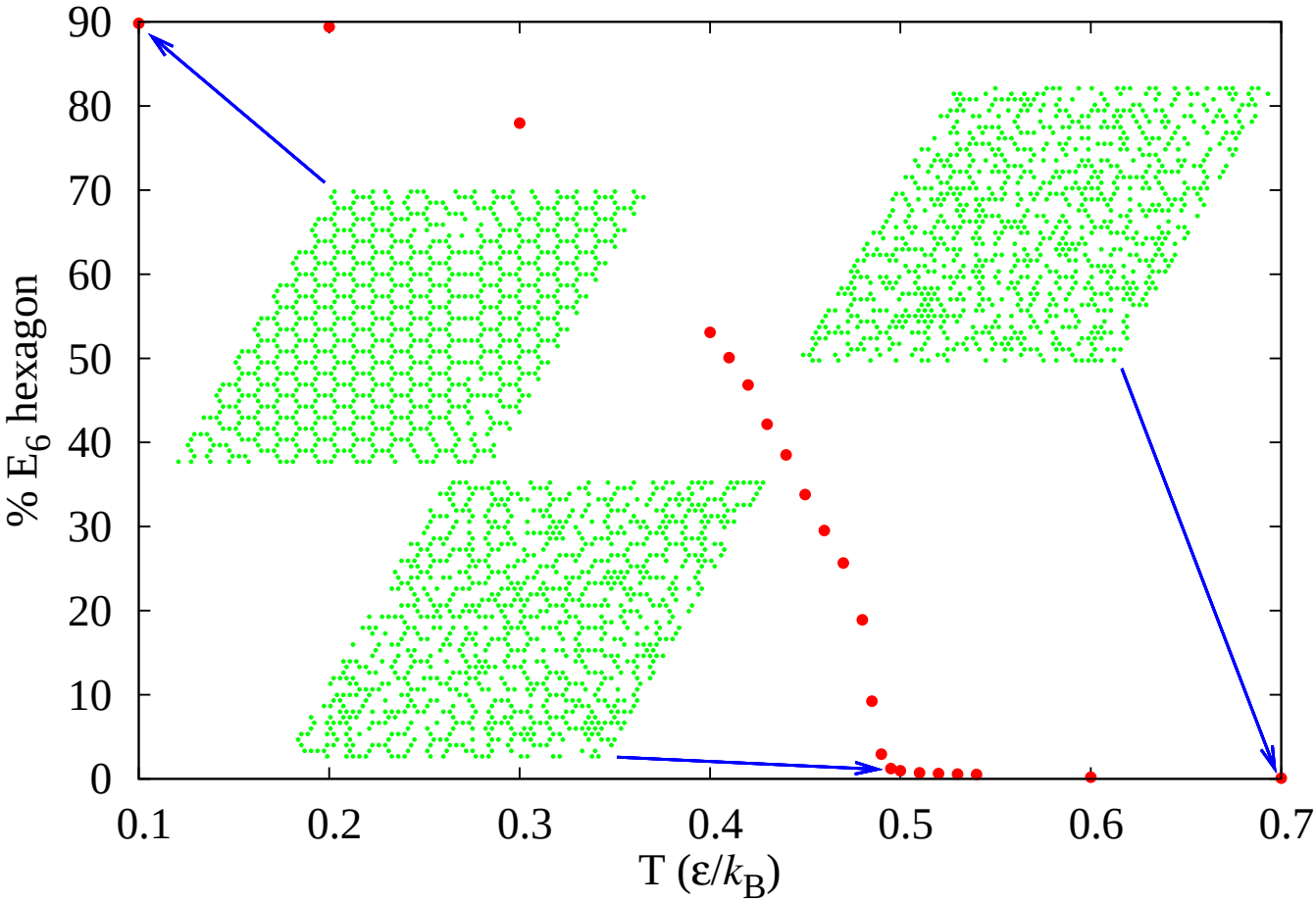

FIG. 15: (Color online) Percentage of E_6 hexagons as a function of temperature at $\rho = 0.4$. The ground state site configurations are also shown at the temperatures $T = 0.1\epsilon/k_B$, $T = 0.7\epsilon/k_B$, and $T = 0.495\epsilon/k_B$. $T_c = 0.495\epsilon/k_B$ is the transition temperature. Each point is an average over 100 different runs.

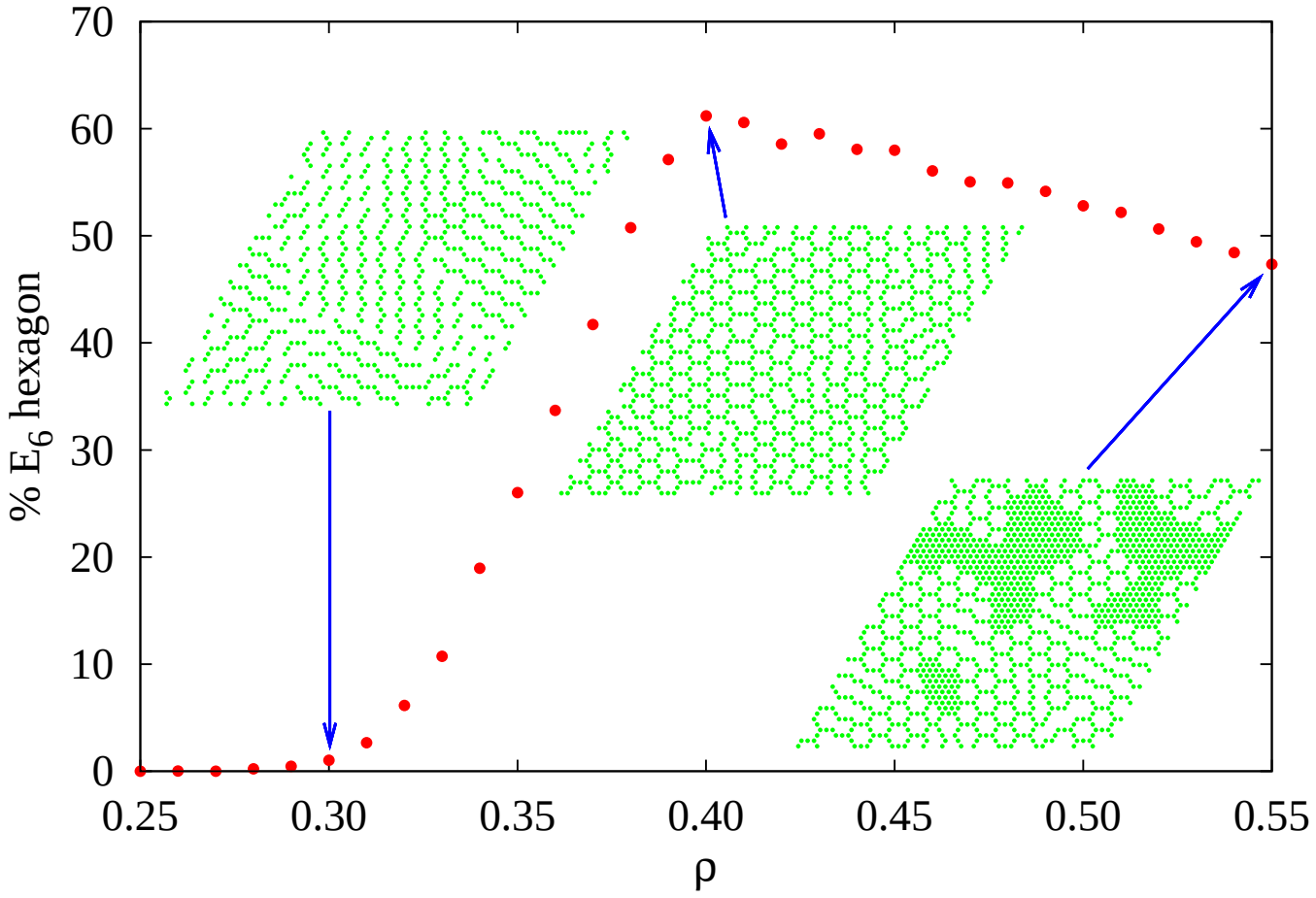

FIG. 16: (Color online) Percentage of E_6 hexagons as a function of particle density ρ at temperature $T = 0.001\epsilon/k_B$. Here also each point is an average over 100 different runs. The ground state site configurations are also shown at $\rho = 0.30$, $\rho = 0.40$, and $\rho = 0.55$. Hexagons start to appear at $\rho = 0.30$, peaks at $\rho = 0.40$, and decrease slightly after that.

[1] Hiroyuki Tanaka, Takaomi Nakagawa, and Tomoji Kawai, Surf. Sci. **364**, L575 (1996); Tomoji Kawai, Hiroyuki Tanaka, and Takaomi Nakagawa, Surf. Sci. **386**, 124 (1997).

[2] J. Voetsa, J. W. Gerritsen, R. F. P. Grimbergen and H. van Kempen, Surf. Sci. **399**, 316 (1998); F. Schreiber, A. Eberhardt, T. Y. B. Leung, P. Schwartz, S. M. Wetterer, D. J. Lavrich, L. Berman, P. Fenter, P. Eisenberger, and G. Scoles, Phys. Rev. B **57**, 12476 (1998).

[3] Tien-Tzu Liang, Hiroaki Azehara, Takao Ishida, Wataru Mizutani, and Hiroshi Tokumoto, Synthetic Metals **140**, 139 (2004).

[4] Mathieu Abel, Vincent Oison, Mathieu Koudia, and Louis Porte, Phys. Rev. B **77**, 085410 (2008).

[5] J. A. Miwa, F. Cicoira, J. Lipton-Duffin, D. F. Perepichka, C. Santato, and F. Rosei, Nanotechnology **19**, 424021 (2008).

[6] H. Liddar, J. Li, A. Neogi, P. B. Neogi, A. Sarkar, S. Cho, and H. Morkoç, Appl. Phys. Lett. **92**, 013309 (2008).

[7] Elad D. Mentovich, Itshak Kalifa, Alexander Tsukernik, Ariel Caster, Natalie Rosenberg-Shraga, Hanit Marom, Michael Gozin, and Shachar Richter, Small **4**, 55 (2008).

[8] Oded Hod, Roi Baer, and Eran Rabani, J. Phys.: Condens. Matter **20**, 383201 (2008).

[9] Seema Singh, Darryl Y. Sasaki, Joseph Cesarano III, and Alan J. Hurd, Thin Solid Films **339**, 209 (1999).

[10] R. Plass, N. C. Bartelt, and G. L. Kellogg, J. Phys.: Condens. Matter **14**, 4227 (2002).

[11] Rachel K. Smith, Penelope A. Lewis, and Paul S. Weiss, Prog. Surf. Sci. **75**, 1 (2004).

[12] Nitin Kumar and Jong-in Hahm, Langmuir, **21**, 6652 (2005).

[13] Sivashankar Krishnamoorthy, Marc Antonius Friedrich Van den Boogaart, Juergen Brugger, Cyrille Hibert, Raphael Pugin, Christian Hinderling, and Harry Heinzelmann, Adv. Mater. **20**, 3533 (2008).

[14] Greg Pawin, Kin L. Wong, Ki-Young Kwon, and Ludwig Bartels, Science **313**, 961 (2006).

[15] M. M. Hurley and Sherwin J. Singer, Phys. Rev. B **46**, R5783 (1992). Unfortunately, this paper denotes by J the lattice gas energy, leading to potential confusion with the Ising model exchange parameter and consequent errors by factors of 4.

[16] Antitsa D. Stoycheva and Sherwin J. Singer, Phys. Rev. Lett. **84**, 4657 (2000); Phys. Rev. E **65**, 036706 (2002).

[17] M. Ifti, Q. Li, C. M. Soukoulis, and M. J. Velgakis, Modern Phys. Lett. B **15**, 895 (2001).

[18] Pablo M. Gleiser, Francisco A. Tamarit, and Sergio A. Cannas, Phys. Rev. B **68**, 134401 (2003).

[19] Sergio A. Cannas, Mateus F. Michelon, Daniel A. Stariolo, and Francisco A. Tamarit, Phys. Rev. B **73**, 184425 (2006).

[20] Santiago A. Pighín and Sergio A. Cannas, Phys. Rev. B **75**, 224433 (2007).

[21] A. Joknys and E. E. Tornau, J. Magn. Magn. Mater. **321**, 137 (2009).

[22] S. M. Patchedjiev, J. P. Whitehead, and K. De'Bell, J. Phys.: Condens. Matter **19**, 196207 (2007).

[23] Yan Mu and Yu-qiang Ma, Phys. Rev. B **67**, 014110 (2003).

[24] A. Imperio and L. Reatto, J. Phys.: Condens. Matter **16**, S3769 (2004).

[25] J. Ricardo de Sousa and N. S. Branco, Phys. Rev. B **72**, 134421 (2005).

[26] Alan B. de Oliveira and Marcia C. Barbosa, J. Phys.: Condens. Matter **17**, 399 (2005).

[27] R. R. Levitskii, S. I. Sorokov, and A. S. Vdovych, Ferroelectrics **316**, 111 (2005).

[28] D. Pini, A. Parola, and L. Reatto, J. Phys.: Condens. Matter **18**, S2305 (2006).

[29] Bo Yang, Tejodher Muppidi, Vidvuds Ozolin, and Mark Asta, Phys. Rev. B **77**, 205408 (2008).

[30] A. J. Archer, C. Ionescu, D. Pini, and L. Reatto, J. Phys.: Condens. Matter **20**, 415106 (2008).

[31] T. L. Einstein, Langmuir **7**, 2520 (1991).

[32] T. L. Einstein, in Physical Structure of Solid Surfaces, edited by W. N. Unertl (Elsevier, Amsterdam, 1996), Handbook of Surface Science, Vol. 1, p. 577.

[33] S. Ostlund and A. N. Berker, Phys. Rev. B **21**, 5410 (1980); Robert G. Caflisch and A. Nihat Berker, Phys. Rev. B **29**, 1279 (1984).

[34] L. Österlund, M. Ø. Pedersen, I. Stensgaard, E. Lægsgaard, and F. Besenbacher, Phys. Rev. Lett. **83**, 4812 (1999).

[35] A. Bogicevic, S. Ovesson, P. Hyldgaard, B. I. Lundqvist, H. Brune, and D. R. Jennison, Phys. Rev. Lett. **85**, 1910 (2000).

[36] Weiwei Luo and Kristen A. Fichthorn, Phys. Rev. B **72**, 115433 (2005).

[37] J.-S. McEwen, S. H. Payne, and C. Stampfl, Chem. Phys. Lett. **361**, 317 (2002); Catherine Stampfl, Catalysis Today **105**, 17 (2005); Mikael Borg, Catherine Stampfl, Anders Mikkelsen, Johan Gustafson, Edvin Lundgren, Matthias Scheffler, and Jesper N. Andersen, Chem. Phys. Chem. **6**, 1923 (2005).

[38] K. Berland, T. L. Einstein, and P. Hyldgaard, Phys. Rev. B **80**, 155431 (2009).

[39] Jascha Repp, Francesca Moresco, Gerhard Meyer, Karl-Heinz Rieder, Per Hyldgaard, and Mats Persson, Phys. Rev. Lett. **85**, 2981 (2000).

[40] N. Knorr, H. Brune, M. Epple, A. Hirstein, M. A. Schneider, and K. Kern, Phys. Rev. B **65**, 115420 (2002).

[41] P. Hyldgaard and T. L. Einstein, Europhys. Lett. **59**, 265 (2002); J. Cryst. Growth **275**, e1637 (2005).

[42] L. Diekhöner, M. A. Schneider, A. N. Baranov, V. S. Stepanyuk, P. Bruno, and K. Kern, Phys. Rev. Lett. **90**, 236801 (2003); N. N. Negulyaev, V. S. Stepanyuk, L. Niebergall, W. Hergert, H. Fangohr, and P. Bruno, Phys. Rev. B **74**, 035421 (2006); N. N. Negulyaev, V. S. Stepanyuk, L. Niebergall, P. Bruno, W. Hergert, J. Repp, K.-H. Rieder, and G. Meyer, Phys. Rev. Lett. **101**, 226601 (2008).

[43] M. E. J. Newman and G. T. Barkema, *Monte Carlo Methods in Statistical Physics* (Oxford University Press, New York, 1999), pp. 138–143.

[44] There is a simple trick to allow us to represent the triangular lattice as the notationally-simpler square lattice in our algorithm. By adding next-nearest-neighbor diagonal bonds along one diagonal of each square on a square lattice, we can produce a lattice which has the same topology as the regular triangular lattice; a simple shear will take the lattice into a

triangular one. Since it is only the topology of the lattice that matters here, we can thus represent, without approximation, a triangular lattice as a square lattice. The only thing that changes is which sites are nearest-neighbors of which others. See Ref. 43 for more information.

[45] Jonathan Wyrick, Dae-Ho Kim, Dezheng Sun, Zhihai Cheng, Kristian Berland, Yong Su Kim, Eli Rotenberg, Wenhao Lu, Yeming Zhu, Miaomiao Luo, Per Hyldgaard, T. L. Einstein, and Ludwig Bartels, supplemental material of submitted manuscript.